ACADEMIC PRESS

Available online at www.sciencedirect.com

SCIENCE DIRECT®

Journal of Sound and Vibration 263 (2003) 831–851

JOURNAL OF SOUND AND VIBRATION

www.elsevier.com/locate/jsvi

Analysis and optimization of trimorph ring transducers

Shuo-Hung Chang*, Jann-Fang Lin

Department of Mechanical Engineering, National Taiwan University, Taipei, Taiwan, ROC

Received 19 January 2001; accepted 15 July 2002

Abstract

The Kirchoff–Love plate theory and electroelasticity theory are combined to simulate the dynamic behaviors of the trimorph ring transducers under different boundary conditions. The transducer consists of an isotropic elastic ring laminated between two identical piezoelectric rings. Their electric current response, resonant frequencies, antiresonant frequencies and electromechanical coupling coefficients (EMCCs) are theoretically formulated and studied by numerical simulation. Also, the resonant frequencies and their corresponding mode shape are simulated by the finite element modelling to verify the theoretical results. Finally, to obtain the maximum energy conversion efficiency, the dynamic EMCC is optimized by varying the proportion of piezoelectric and elastic parts. It is shown that the dynamic EMCC depends on geometric thickness and radii ratios. Optimum settings for a particular transducer to reach the maximum dynamic EMCC are found for different boundary conditions. The trimorph ring transducer for the fixed inner and free outer surfaces boundary condition has slightly lower resonant and anti-resonant frequencies, and larger EMCCs than that for the free inner and fixed outer surfaces boundary condition does.

1. Introduction

The strong electromechanical coupling effects of piezoelectric materials make themselves become one of the most important intelligent materials in terms of the abilities of actuation, sensing and control. The devices based on piezoelectricity have been expanded rapidly in applications from ultrasonic transducer [1], actuator [2], vibratory gyrosensor [3], and optical scanner [4], to precision positioning mechanism [5].

Many applications using ring piezoelectric structures can be found for resonator [6], ring transducer [7], moving actuator [8], and piezomotor [9]. Research results on the vibration characteristics of piezoelectric ring structure include finite-element method (FEM) [10], theoretical

*Corresponding author. Tel.: 886-2-2363-3863; fax: 886-2-2363-1755.
E-mail address: shchang@ccms.ntu.edu.tw (S.-H. Chang).

0022-460X/03/$ - see front matter
PII: S0022-460X(02)01076-3

model on thickness mode vibration on single ring [11], and other theoretical model on laminated ring, plates [12–15], and bimorph disks [16]. The laminated elastic and piezoelectric rings were used as the dynamic focusing lens [17] and variable-focus mirror [18]. Those works focus on resonant frequencies, mode shapes, and sensitivity of sensor or ability of actuator. However, to measure the practicality of a piezoelectric transducer, the efficiency of energy conversion between mechanical and electric ones is an essential index. All above studies pay little attention on it.

In this article, the piezoelectric trimorph ring transducer under study consists of an isotropic elastic ring laminated between two identical piezoelectric rings. The inner and outer radii are same for elastic and piezoelectric layers. The trimorph ring is mechanically supported either at the inner or outer radius to form the fixed–free, free–fixed, and fixed–fixed boundary conditions. The Poisson's ratios of piezoelectric and elastic layers are treated not the same. The piezoelectric rings are fully covered by electrode, polarized in thickness direction and isotropic transversely. The elastic ring is treated as the common electrode to piezoelectric rings and the electric potential applied to both of the piezoelectric rings are identical. Under sinusoidal electric excitations, one piezoelectric ring expands and the other contracts both in the radial direction. Thus, the major motion of laminated trimorph ring transducer is the bending vibration owing to unequal extensions of piezoelectric and elastic rings.

To study characteristics of the trimorph ring transducer, an electroelastic laminated plate theory was developed first to analyze its dynamic behaviors such as electric current response, resonant frequencies, antiresonant frequencies and electromechanical coupling coefficients (EMCCs). This theory was formulated by combining the equilibrium equations, the geometric relationships, the constitutive relations and the electrostatic equations. The piezoelectric effects were included with the use of the Kirchhoff–Love plate theory. The distribution of electric potential and electric displacement in the thickness direction for piezoelectric layer were assumed quadratic and constant with respect to the thickness co-ordinate, respectively. These characteristics were therefore numerically evaluated for different values of geometric variables, such as thickness and radius ratios of the piezoelectric and elastic layers. Also, the FEM was applied to simulate and verify the vibration characteristics obtained by previous numerical evaluation. Finally, to attain highest energy conversion efficiency of the trimorph ring transducer was realized by changing the proportion of piezoelectric and elastic parts to reach the maximum dynamic EMCC. The optimum setting for a particular trimorph ring is found as an example.

2. Electroelastic theory

A complete electroelastic theory consists of the equilibrium equations, the geometric relationships, the constitutive relations and the electrostatic equations. For piezoelectric materials of class 6 mm and polarized in the thickness direction $\alpha_3(z)$, the constitutive relations are [19]:

$$
\begin{aligned}
S_{11} &= s_{11}^E T_{11} + s_{12}^E T_{22} + s_{13}^E T_{33} + d_{31} E_3,\\
S_{22} &= s_{12}^E T_{11} + s_{11}^E T_{22} + s_{13}^E T_{33} + d_{31} E_3,\\
S_{33} &= s_{13}^E (T_{11} + T_{22}) + s_{33}^E T_{33} + d_{33} E_3,\\
S_{23} &= s_{44}^E T_{23} + d_{15} E_2,
\end{aligned}
$$

$$
\begin{aligned}
S_{13} &= s_{44}^{E} T_{13} + d_{15} E_1, \\
S_{12} &= s_{66}^{E} T_{12}, \\
D_1 &= d_{15} T_{13} + \varepsilon_{11}^{T} E_1, \\
D_2 &= d_{15} T_{23} + \varepsilon_{11}^{T} E_2, \\
D_3 &= d_{31}(T_{11} + T_{22}) + d_{33} T_{33} + \varepsilon_{33}^{T} E_3,
\end{aligned} \tag{1}
$$

where S_{ij}, T_{ij}, D_i and E_i denote the components of strain, stress, electric displacement and electric fields, respectively, and s_{ij}^{E}, d_{ij} and ε_{ij}^{T} denote the elastic compliance constants at constant electric field, the piezoelectric constants, and the dielectric constant at constant stress field, respectively. The constitutive relations for the isotropic elastic materials are

$$
\begin{aligned}
S_{11} &= \frac{1}{E}(T_{11} - \nu_m T_{22} - \nu_m T_{33}), \\
S_{22} &= \frac{1}{E}(T_{22} - \nu_m T_{11} - \nu_m T_{33}), \\
S_{33} &= \frac{1}{E}(T_{33} - \nu_m T_{11} - \nu_m T_{22}), \\
S_{23} &= \frac{2(1+\nu_m)}{E} T_{23}, \\
S_{13} &= \frac{2(1+\nu_m)}{E} T_{13}, \\
S_{12} &= \frac{2(1+\nu_m)}{E} T_{12},
\end{aligned} \tag{2}
$$

where E and ν_m are Young's modulus and Poisson's ratio of the elastic material. The general electrostatic equations are

$$
\begin{aligned}
\nabla \cdot \vec{D} &= 0, \\
\vec{E} &= -\nabla \psi,
\end{aligned} \tag{3}
$$

where ψ is the electric potential. To analyze the flexure problem precisely, we should choose the mutually perpendicular lines on the middle surface as co-ordinates α_1 and α_2, and the normal to the middle surface as the third co-ordinate $\alpha_3(z)$. However, the piezoelectric–elastic actuator displaces infinitesimally, so the equilibrium equations for flat plates without surface traction in cylindrical co-ordinates r, θ and z, shown in Fig. 1, are

$$
\begin{aligned}
&\frac{\partial T_{11}}{\partial r} + \frac{1}{r}(T_{11} - T_{22}) + \frac{1}{r}\frac{\partial T_{12}}{\partial \theta} + \frac{\partial T_{13}}{\partial z} = \rho \frac{\partial^2 U_r}{\partial t^2}, \\
&\frac{\partial T_{21}}{\partial r} + \frac{1}{r}\frac{\partial T_{22}}{\partial \theta} + \frac{\partial T_{23}}{\partial z} + \frac{2T_{21}}{r} = \rho \frac{\partial^2 U_\theta}{\partial t^2}, \\
&\frac{\partial T_{31}}{\partial r} + \frac{1}{r}\frac{\partial T_{32}}{\partial \theta} + \frac{\partial T_{33}}{\partial z} + \frac{T_{31}}{r} = \rho \frac{\partial^2 U_z}{\partial t^2},
\end{aligned} \tag{4}
$$

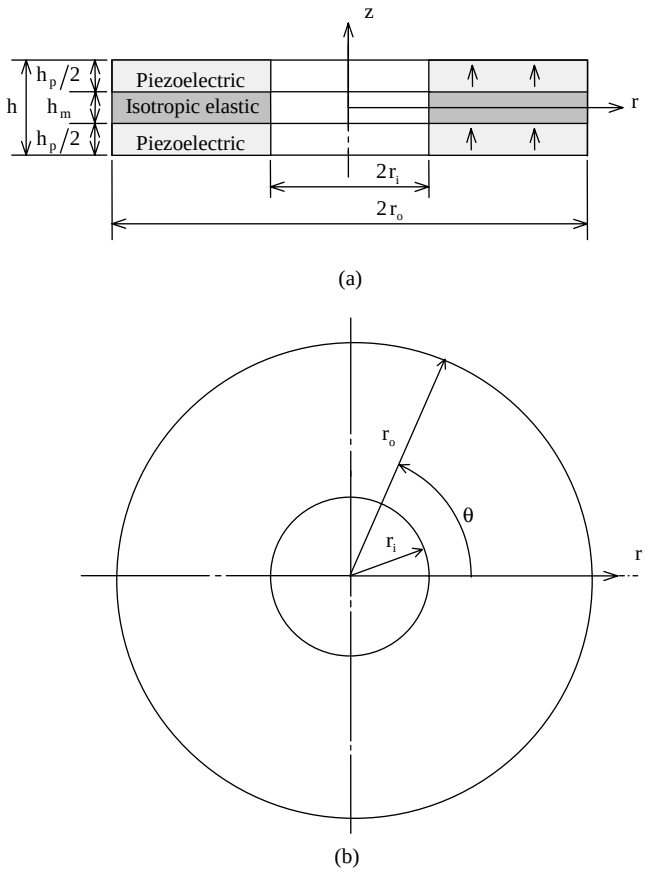

Fig. 1. Configuration of the trimorph ring transducer. (a) cross section, and (b) top view.

where U_i and ρ are the components of displacement and material density, respectively. The geometric relationships are

$$
\begin{aligned}
S_{11} &= \frac{\partial U_r}{\partial r}, \\
S_{22} &= \frac{1}{r}\frac{\partial U_\theta}{\partial \theta} + \frac{U_r}{r}, \\
S_{33} &= \frac{\partial U_z}{\partial z}, \\
S_{12} &= \frac{1}{r}\frac{\partial U_r}{\partial \theta} - \frac{U_\theta}{r} + \frac{\partial U_\theta}{\partial r}, \\
S_{13} &= \frac{\partial U_r}{\partial z} + \frac{\partial U_z}{\partial r}, \\
S_{23} &= \frac{\partial U_\theta}{\partial z} + \frac{1}{r}\frac{\partial U_z}{\partial \theta}.
\end{aligned} \tag{5}
$$

To simplify this electroelastic problem, four assumptions are proposed. The first two are Kirchhoff–Love hypotheses used in the classical plate theory for non-electric plates and the others are particularly used for piezoelectric materials. The first hypothesis is that the normal stress acting on the surface elements parallel to the middle surface is small and can be neglected as compared to other stresses:

$$T_{33} = 0. \tag{6}$$

The second hypothesis is that a line normal to the middle surface before deformation remains perpendicular to the strained surface and is not extended after deformation:

$$S_{13} = S_{23} = 0. \tag{7}$$

The third hypothesis is that the electric potential varies with thickness by the quadratic relation [20]

$$\psi = \psi^0 + z\psi^1 + z^2\psi^2, \tag{8}$$

where ψ^0, ψ^1, and ψ^2 are coefficients of z term and independent of z, in which the superscript n denotes the nth power term in the co-ordinate z. The fourth hypothesis is that the electric displacement is constant along the plate thickness:

$$D_3 = D_3^0, \tag{9}$$

where D_3^0 is a constant independent of z. Besides, the membrane forces N_{ij} and bending moments M_{ij}, where $i, j = r, \theta$, are considered instead of stress in this electroelastic plate theory and are defined as

$$N_{ij} = \int_z T_{ij}\,\mathrm{d}z, \quad M_{ij} = \int_z T_{ij} z\,\mathrm{d}z. \tag{10}$$

Thus, the general electroelastic laminate plate theory can be derived from Eqs. (1) to (10), but only those relations for a particular piezoelectric/elastic rings are shown in this paper. Fig. 1 shows the trimorph ring transducer with outer diameter $2r_o$ and inner diameter $2r_i$. It consists of an isotropic elastic ring laminated between two identical piezoelectric rings, which their radii equal to elastic ring. The major faces of piezoelectric rings are fully covered by thin electrodes whose thickness can be neglected. They are polarized in thickness direction as shown by the arrowheads in Fig. 1 and isotropic transversely. The elastic ring is treated as the common electrode to those piezoelectric rings and the electric potentials applied to these two piezoelectric rings are equal. If the middle plane of the ring is chosen as the reference plane, the electric boundary conditions can be expressed as

$$\psi|_{z=h/2} = \psi|_{z=-h/2} = V, \quad \psi|_{z=h_m/2} = \psi|_{z=-h_m/2} = -V, \tag{11}$$

where V is the applied voltage. Under this configuration and the applied electric potential, one of piezoelectric rings extends while the other contracts. Thus, the major motion of the ring is a bending vibration under a sinusoidal electric excitation. In addition, the dynamic responses in the

θ direction is omitted due to the axis-symmetry:

$$\frac{\partial f}{\partial \theta} = 0, \tag{12}$$

where f is the arbitrary physical quantity of the trimorph ring transducer. Due to the symmetry of the ring, extensional motion in the middle plane will not occur, i.e.,

$$U_r|_{z=0} = 0. \tag{13}$$

To determine the dynamic responses, boundary conditions of the system are specified here. For the fixed inner and free outer circumferential surfaces of the laminated trimorph ring transducer, the mechanical boundary conditions are:

$$\begin{aligned} &U_z|_{r=r_i} = 0, \quad \left.\frac{\partial U_z}{\partial r}\right|_{r=r_i} = 0, \\ &N_{rz}|_{r=r_o} = 0, \quad M_{rr}|_{r=r_o} = 0, \end{aligned} \tag{14}$$

where r_i, r_o are the inner and outer radii, respectively.

Moreover, for the free inner and fixed outer circumferential surfaces of the laminated trimorph ring transducer, the mechanical boundary conditions are

$$\begin{aligned} &N_{rz}|_{r=r_i} = 0, \qquad M_{rr}|_{r=r_i} = 0, \\ &U_z|_{r=r_o} = 0, \qquad \left.\frac{\partial U_z}{\partial r}\right|_{r=r_o} = 0. \end{aligned} \tag{15}$$

And for the fixed inner and fixed outer circumferential surfaces of the laminated trimorph ring transducer, the mechanical boundary conditions are

$$\begin{aligned} &U_z|_{r=r_i} = 0, \quad \left.\frac{\partial U_z}{\partial r}\right|_{r=r_i} = 0, \\ &U_z|_{r=r_o} = 0, \quad \left.\frac{\partial U_z}{\partial r}\right|_{r=r_o} = 0. \end{aligned} \tag{16}$$

Combining Eqs. (1)–(13), the equilibrium equations can be greatly simplified. The tedious procedure is briefly stated below. From Kirchhoff–Love hypotheses, the displacements in the r, θ, z directions, U_r, U_θ, U_z at arbitrary point of the trimorph ring transducer can be expressed as

$$\begin{aligned} U_r(r,\theta,z) &= u_r(r,\theta) + z\beta_r(r,\theta), \\ U_\theta(r,\theta,z) &= u_\theta(r,\theta) + z\beta_\theta(r,\theta), \\ U_z(r,\theta,z) &= u_z(r,\theta), \end{aligned} \tag{17}$$

where u_r, u_θ, u_z are the displacements in the r, θ and z directions of the reference plane, respectively, and

$$\beta_r = -\frac{\partial u_z}{\partial r}, \quad \beta_\theta = -\frac{1\partial u_z}{r\,\partial \theta}, \tag{18}$$

Using cylindrical co-ordinates and substituting Eqs. (12), (13) and (17) into Eq. (5), then strains are expressed as

$$S_{11} = zk_{rr},$$
$$S_{22} = zk_{\theta\theta}, \tag{19}$$

where k_{ii}, $i = r$, θ denote the bending strains and are defined as

$$k_{rr} = -\frac{\partial^2 u_z}{\partial r^2},$$
$$k_{\theta\theta} = -\frac{1\partial u_z}{r\,\partial r}. \tag{20}$$

To simplify equilibrium equations, we first change co-ordinates of Eq. (4) into cylindrical ones and substitute Eqs. (6), (7), (12), (13) and (17) into Eq. (4). We then integrate Eq. (4) with respect to z, and multiply Eq. (4) with z and integrate results with respect to z. Eq. (10) is used to make derived equations more clearly. Besides, the ring laminate in this paper is thin and the rotating inertia is omitted. After the above procedures, the equilibrium equations can be expressed as

$$\frac{1}{r}\frac{\partial}{\partial r}\left\{r\left[\frac{\partial M_{rr}}{\partial r} + \frac{1}{r}(M_{rr} - M_{\theta\theta})\right]\right\} = R_0\frac{\partial^2 u_z}{\partial t^2}, \tag{21}$$

where

$$R_0 = \rho_m h_m + \rho_p h_p \tag{22}$$

and ρ_m and ρ_p are the density of elastic and piezoelectric material, respectively. Also, we can take integration of Eq. (10) by combining Eqs. (1)–(3), (8), (9), (19) and (20), using cylindrical co-ordinates, the bending moments can be expressed as

$$\begin{bmatrix} M_{rr} \\ M_{\theta\theta} \end{bmatrix} = \begin{bmatrix} D_{11} & D_{12} \\ D_{12} & D_{11} \end{bmatrix}\begin{bmatrix} k_{rr} \\ k_{\theta\theta} \end{bmatrix} + \begin{bmatrix} F_{11} \\ F_{11} \end{bmatrix} V, \tag{23}$$

where

$$D_{11} = \frac{E_m h_m^3}{12(1-v_m^2)} + \frac{(1-B+Bv_p)(h^3-h_m^3)}{12s_{11}^E(1-v_p^2)(1-2B)} - \frac{B(h+h_m)(h^2-h_m^2)}{16s_{11}^E(1-v_p)(1-2B)},$$
$$D_{12} = \frac{E_m v_m h_m^3}{12(1-v_m^2)} + \frac{(v_p+B-Bv_p)(h^3-h_m^3)}{12s_{11}^E(1-v_p^2)(1-2B)} - \frac{B(h+h_m)(h^2-h_m^2)}{16s_{11}^E(1-v_p)(1-2B)},$$
$$F_{11} = \frac{d_{31}(h+h_m)}{s_{11}^E(1-v_p)}, \tag{24}$$

and

$$B = \frac{d_{31}^2}{\varepsilon_{33}^T s_{11}^E(1-v_p)} = \tfrac{1}{2}k_p^2,$$
$$v_p = -\frac{s_{12}^E}{s_{11}^E}. \tag{25}$$

where k_p is the planar coupling factor or radial coupling factor for single piezoelectric ring under static radial vibration. Also, the membrane force N_{rz} can be related to the bending moments M_{rr}, $M_{\theta\theta}$ as following:

$$N_{rz} = \frac{\partial M_{rr}}{\partial r} + \frac{1}{r}(M_{rr} - M_{\theta\theta}). \tag{26}$$

Finally, substituting Eqs. (20) and (23) into Eq. (21), the governing equations of the trimorph ring transducer can be expressed as

$$-D_{11}\left(\frac{\partial^4 u_z}{\partial r^4} + \frac{2\partial^3 u_z}{r\ \partial r^3} - \frac{1}{r^2}\frac{\partial^2 u_z}{\partial r^2} + \frac{1}{r^3}\frac{\partial u_z}{\partial r}\right) = R_0\frac{\partial^2 u_z}{\partial t^2}. \tag{27}$$

To analyze the dynamic characteristics of the trimorph ring transducer, we assume the displacement of the reference plane in thickness direction is

$$u_z(r, t) = W_z(r)\mathrm{e}^{\mathrm{j}\omega t}, \tag{28}$$

where ω is the angular frequency of vibration. The general solution, $W_z(r)$, is

$$W_z(r) = [C_1\mathrm{J}_0(\lambda_z r) + C_2\mathrm{I}_0(\lambda_z r) + C_3\mathrm{Y}_0(\lambda_z r) + C_4\mathrm{K}_0(\lambda_z r)], \tag{29}$$

where

$$(\lambda_z)^4 = \frac{R_0}{D_{11}}\omega^2, \tag{30}$$

and J_0 and Y_0 are the Bessel functions of the first and second kinds of order zero, respectively, I_0 and K_0 are the modified Bessel functions of the first and second kinds of order zero, respectively, and λ_z is the frequency parameter.

Define a dimensionless frequency parameter, which relates to frequency parameter as

$$\left(\lambda_z^*\right)^4 \equiv (\lambda_z)^4 \times r_o^4. \tag{31}$$

By substituting Eqs. (19) and (28) into boundary conditions (14) or (15) or (16), the matrix form of algebraic equations including coefficients C_j for different boundary conditions can be written as

$$[A] \cdot \{C\} = \{F\}, \tag{32}$$

where

$$\{C\} = \{C_1, C_2, C_3, C_4\}^{\mathrm{T}}, \tag{33}$$

and $[A]$ is a fourth order square matrix, and $\{F\}$ is a 4×1 matrix. The elements of $[A]$ and $\{F\}$ are listed in the appendix. Coefficients C_j can be found by meeting boundary conditions. The resonant frequencies can be determined by solving

$$\det([A]) = 0. \tag{34}$$

Since the applied voltage V only appeared in $\{F\}$ and is not involved in $[A]$, the resonant frequencies are obviously irrelevant to the applied voltage V.

Besides, The electric current I over a conduction area S_e can be calculated using

$$I = \int_{S_e} \frac{\mathrm{d}D_3^0}{\mathrm{d}t}\,\mathrm{d}S_e. \tag{35}$$

By expressing stresses in terms of displacement, and using Eqs. (1)–(3), (8), (9), (11), and (17), the electric current I would be

$$I = \frac{-j\pi\omega d_{31}(h+h_m)}{2s_{11}^E(1-v_p)}\left[-(r\beta_r)|_{r=r_i}^{r=r_o} + \frac{8d_{31}(1-2B)}{B(h^2-h_m^2)}(r_o^2-r_i^2)V\right], \tag{36}$$

where $j = \sqrt{-1}$.

The anti-resonant frequencies can be determined by solving

$$I = 0. \tag{37}$$

We can infer that the antiresonant frequencies are dependent of the applied voltage V by Eqs. (36) and (37), which is different from the resonant ones.

There are two kinds of electromechanical coupling coefficients (EMCCs) to evaluate the transduction efficiency between electric energy and mechanical energy for a transducer in dynamic state. They are the dynamic electromechanical coupling coefficient k_d and energy electromechanical coupling coefficient k_e. The dynamic electromechanical coupling coefficient k_d is defined by Mason, which takes the formula [21]

$$k_d^2 = \frac{f_a^2 - f_r^2}{f_a^2}, \tag{38}$$

where f_r and f_a are the resonant and antiresonant frequencies at the specified mode number, respectively. However k_d can be only utilized to assess the transfer efficiency near the resonant frequencies, thus, Ulitko proposed the energy electromechanical coupling coefficient k_e as follows:

$$k_e^2 = \frac{U^{(d)} - U^{(sh)}}{U^{(d)}}, \tag{39}$$

where $U^{(d)}$ and $U^{(sh)}$ are the internal energies for the disconnected and short circuits, respectively. The internal energy mainly includes mechanical energy, dielectric energy, and mutual energy for the concerned trimorph systems. The energy electromechanical coupling coefficient k_e is applicable for any frequency including resonant and antiresonant frequencies to evaluate the efficiency of the transducer.

3. Validation of the theory

The procedure described in the previous section is straightforward. The validity of the theory can be verified first by the experiment. The impedance–frequency response experiments for the trimorph ring transducers under both free inner and outer surfaces boundary condition are presented in Ref. [22], which shows agreement between predictions of the theory and experimental measurements on resonant and antiresonant frequencies. One more verification of the theory is to introduce both the piezoelectric layer thickness h_p and applied voltage V equal zero and to compare results with analytical data [23]. In this case, the laminated trimorph ring transducer simply becomes an isotropic elastic ring, and quantities R_0, D_{11}, λ_z in Eqs. (22), (24),

Table 1
Dimensionless resonant parameters $(\lambda_z^*)_r$ of single elastic ring under the fixed inner and fixed outer surfaces boundary condition

	$r_i/r_o = 0.1$		$r_i/r_o = 0.3$		$r_i/r_o = 0.5$		$r_i/r_o = 0.7$	
	Mode 1	Mode 2	1	2	1	2	1	2
Present result	27.32	75.36	45.14	124.8	89.31	246.5	248.8	687.2
Blevins	27.30	75.30	45.20	125.0	89.20	246.0	248.0	686.0

and (30) become

$$R_0 = \rho_m h_m,$$
$$D_{11} = \frac{E h_m^3}{12(1-\nu_m^2)},$$
$$(\lambda_z)^4 = \frac{12\rho_m(1-\nu_m^2)}{E_m h_m^2}\omega^2. \tag{40}$$

Then the resonant frequencies for the fixed inner and fixed outer surfaces boundary condition are governed by the following equation:

$$\Delta = \det\begin{bmatrix} \mathrm{J}_0(\lambda_z r_i) & \mathrm{I}_0(\lambda_z r_i) & \mathrm{Y}_0(\lambda_z r_i) & \mathrm{K}_0(\lambda_z r_i) \\ \mathrm{J}_1(\lambda_z r_i) & -\mathrm{I}_1(\lambda_z r_i) & \mathrm{Y}_1(\lambda_z r_i) & \mathrm{K}_1(\lambda_z r_i) \\ \mathrm{J}_0(\lambda_z r_o) & \mathrm{I}_0(\lambda_z r_o) & \mathrm{Y}_0(\lambda_z r_o) & \mathrm{K}_0(\lambda_z r_o) \\ \mathrm{J}_1(\lambda_z r_o) & -\mathrm{I}_1(\lambda_z r_o) & \mathrm{Y}_1(\lambda_z r_o) & \mathrm{K}_1(\lambda_z r_o) \end{bmatrix} = 0. \tag{41}$$

We solve the algebraic equation numerically by using software MATLAB, and obtain the fundamental and second dimensionless resonant parameters $(\lambda_z^*)_r$. The resonant frequency f_r relates to the dimensionless resonant parameter $(\lambda_z^*)_r$ by

$$f_r = \frac{(\lambda_z^*)_r^2}{2\pi(r_o)^2}\left[\frac{E_m h_m^3}{12\rho_m h_m(1-\nu_m^2)}\right]^{1/2}. \tag{42}$$

The calculated results for different radius ratio r_i/r_o are listed in Table 1. The data found in Ref. [23] are also listed for comparison. It can be easily seen the results are nearly identical. We can also find all the corresponding mode shapes are mushroom-like, of which nodal lines are circulars.

4. Numerical and FEM simulations

To illustrate the dependence of dynamic characteristics on geometric variables such as thickness and radius ratios, the dynamic characteristics of the trimorph ring transducer are numerically calculated. The mathematical software MATLAB is used to handle the tedious computations. Since the first resonant and antiresonant frequencies significantly determine the efficiency of transducers, we here simulate and present their dependence on geometry other than the higher

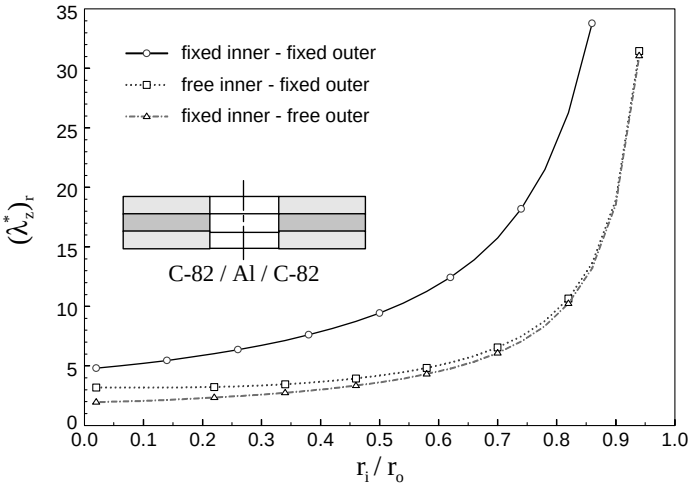

Fig. 2. The first dimensionless resonant parameter $(\lambda_z^*)_r$ versus radius ratio r_i/r_o for different boundary conditions.

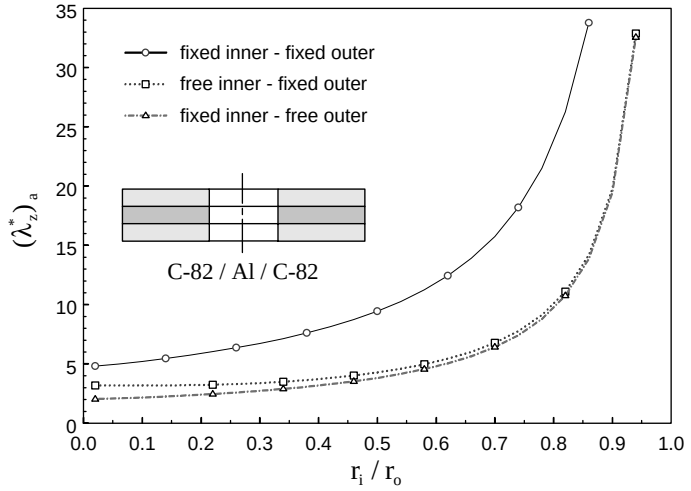

Fig. 3. The first dimensionless antiresonant parameter $(\lambda_z^*)_a$ versus radius ratio r_i/r_o for different boundary conditions.

order ones afterwards. The first dimensionless resonant parameter $(\lambda_z^*)_r$ and antiresonant parameter $(\lambda_z^*)_a$ versus radius ratio r_i/r_o for different boundary conditions are shown in Figs. 2 and 3, respectively. Note that the dimensionless resonant and antiresonant parameters comprise the material property and thickness ratio h_m/h. By Eqs. (30) and (31), the resonant and antiresonant frequencies can be easily calculated for different combinations of ring materials and sizes. For example, Figs. 4 and 5, respectively, show the first resonant frequencies f_r, and antiresonant frequencies f_a, for the fixed inner and free outer surfaces boundary conditions, if piezoceramics Fuji C-82 and metal Al are chosen. The properties of piezoceramics Fuji C-82 and

Table 2
Material properties

Al	
E(GPa)	70
v_m	0.33
$\rho_m(\mathrm{kg/m^3})$	2700
Fuji C-82 PZT	
$\varepsilon_{33}^T/\varepsilon_0$	3400
$d_{31}(\times 10^{-12}\,\mathrm{C/N})$	−260
$Y_{11}^E(=1/s_{11}^E, \mathrm{GPa})$	59
v_p	0.34
$\rho_p(\mathrm{kg/m^3})$	7400

metal Al are listed in Table 2. From Figs. 4 and 5, the values of the first resonant and antiresonant frequencies almost lies between 500 Hz and 100 kHz, however, are quite smaller than those for single piezoelectric ring of the same dimensions—r_i/r_o, h_p. The values of the first resonant and antiresonant frequencies for single piezoelectric ring are all above 15 kHz from impedance measurements [22]. Therefore, trimorph ring transducer greatly reduces in the values of resonant and antiresonant frequencies, which implies it could be operated at lower exciting frequency. This feature inherent in trimorph ring transducer gains an advantage over other ones. From Figs. 2 and 3, the tendencies of resonant and antiresonant parameters are quite in the same way, which monotonically increase as r_i/r_o increases. And, the antiresonant parameters are always lager than the resonant ones in value at same geometric dimensions for all kinds of boundary conditions except the fixed inner and fixed outer surfaces boundary condition, which implies the antiresonant frequencies are all similarly larger than the resonant ones in value at same geometric dimensions, for example, shown in Figs. 4 and 5. Moreover, the resonant and antiresonant parameters for the fixed inner and fixed outer surfaces boundary condition are the largest, but only little difference in value for the other two boundary conditions. For the fixed inner surface and fixed outer surface rings, the displacements of any location of the ring are analytically shown vanished from Eqs. (16), (28), (29) and (32). It results in the identical resonant and antiresonant frequencies and EMCC to be zero. In addition, from Figs. 4 and 5, the resonant and antiresonant frequencies not only monotonically increase as r_i/r_o increases but also do as h_m/h increases. Meanwhile, we also use the FEM software ABAQUS to simulate those cases. The trimorph ring transducer is modeled in 420 solid elements with 2485 nodes, which element types of C3D20R for elastic material and C3D20RE for piezoelectric material. The first four resonant frequencies and their corresponding mode shapes for $r_i/r_o = 0.5$, $h_m/h = 0.05$, and different boundary conditions are shown in Figs. 6–8, respectively. The FEM simulation accumulates much more resonant and antiresonant frequencies, which comprise the ones that cannot be excited by electric potential, for example, modes 2–4 in Figs. 6–8. It can be seen that the mode shapes are almost similar to those of single elastic plate for the same boundary condition except that their corresponding resonant frequencies are largely smaller in values. Also, the first resonant frequencies acquired by FEM simulation are in 5% deviation compared with those obtained by numerical simulation. The second to fourth

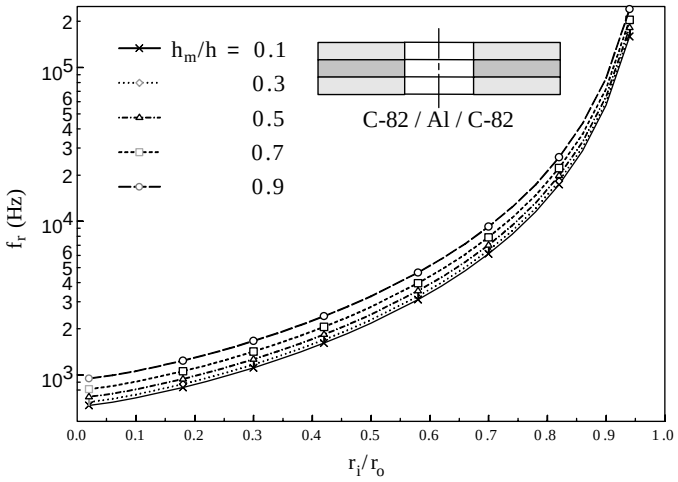

Fig. 4. The first resonant frequency f_r versus thickness ratio h_m/h and radius ratio r_i/r_o for the fixed inner and free outer surfaces boundary condition.

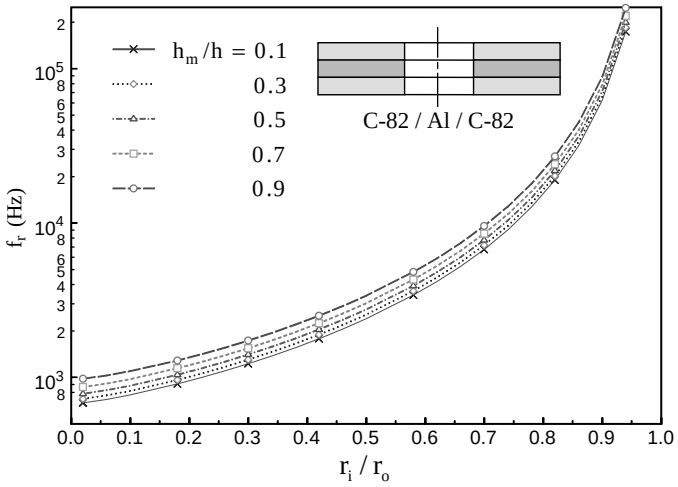

Fig. 5. The first antiresonant frequency f_a versus thickness ratio h_m/h and radius ratio r_i/r_o for the fixed inner and free outer surfaces boundary condition.

resonant frequencies are caused by bending of the trimorph itself, not by bending of unequal extensions of piezoelectric and elastic rings comprised the trimorph. Therefore, they cannot be excited by electric potential, in other words, would not form minimum values in the impedance-frequency response diagram and only the mode shapes with circular nodal lines can be excited by electric potential. This phenomenon interprets the overall bending motion due to unequal extensions of piezoelectric and elastic rings dominates. Similarly, the antiresonant frequencies and their corresponding mode shapes are available by FEM, of which the values are larger than those of resonant frequencies and the corresponding mode shapes are almost the same as those of

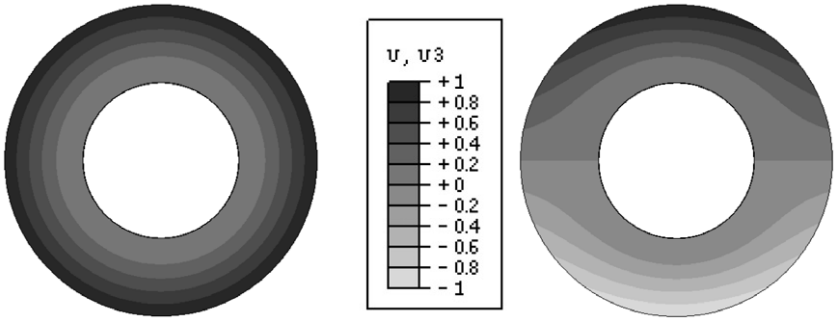

(a) the first resonant frequency: $f_r = 1350.6$ Hz

(b) the second resonant frequency: $f_r = 1358.9$ Hz

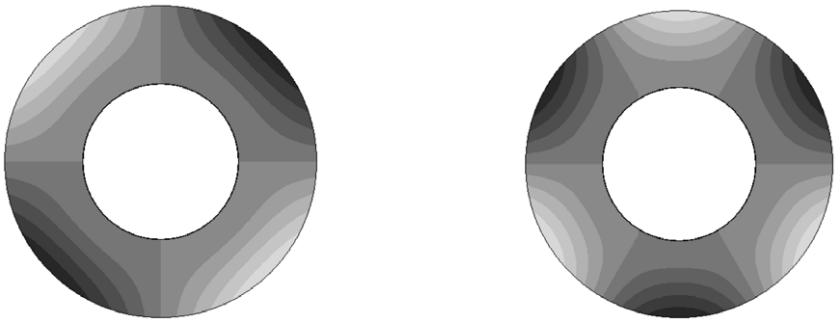

(c) the third resonant frequency: $f_r = 1443.5$ Hz

(d) the fourth resonant frequency: $f_r = 1753.2$ Hz

Fig. 6. The mode shapes with their corresponding resonant frequencies for the fixed inner and free outer surfaces boundary condition.

resonant frequencies except magnitude ratios of deformation. We can also calculate the dynamic EMCC by hand for this particular geometric scale from the frequencies obtained from FEM, however, it need to distinguish the resonant and antiresonant frequencies, which can be really excited by electric potential, from all the simulated values. Besides, it should run FEM program once again to obtain the resonant frequencies, antiresonant frequencies and dynamic EMCCs for another different geometric scale and search the maximum optimized value of them. Therefore, the analytical theory with numerical simulation just predicts resonant and antiresonant frequencies, and easily acquires dynamic and energy EMCCs. The non-dimensional electric current responses of the same transducer for $r_i/r_o = 0.5$, $h_m/h = 0.5$ under different exciting frequency parameters for different boundary conditions are shown in Fig. 9. In this figure, we can see many relative maximums and minimums appeared in sequence. The maximum ones like "peaks" represent that the transducer largely and diversely displaces, which lead to almost zero impedance, and the corresponding frequencies are resonant frequencies at the specified mode number. On the contrary, the minimum ones like "valleys" represent that the transducer also largely and diversely displaces, but lead to almost zero current, and the corresponding frequencies

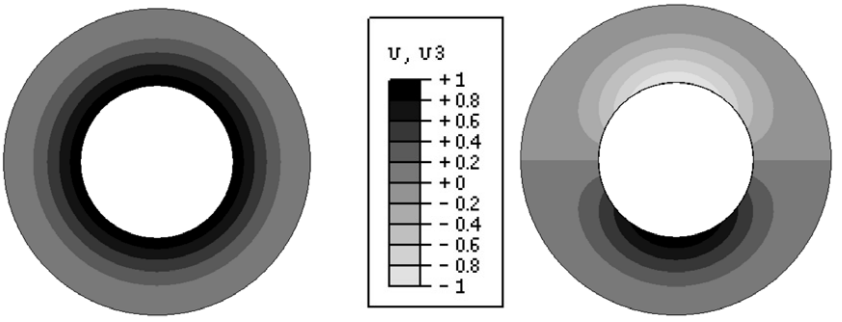

(a) the first resonant frequency: $f_r = 1745.1$ Hz

(b) the second resonant frequency: $f_r = 2111.0$ Hz

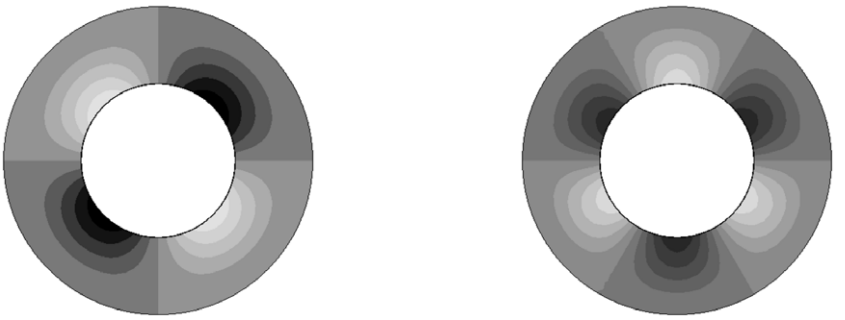

(c) the third resonant frequency: $f_r = 3049.6$ Hz

(d) the fourth resonant frequency: $f_r = 4413.5$ Hz

Fig. 7. The mode shapes with their corresponding resonant frequencies for the free inner and fixed outer surfaces boundary condition.

are antiresonant frequencies, which follow the corresponding resonant frequencies. The dynamic and energy EMCCs of the same transducer for $r_i/r_o = 0.5$, $h_m/h = 0.5$ under different exciting frequency parameters for different boundary conditions are shown in Fig. 10. In this figure, we can see the dynamic EMCCs k_d, which are the points plotted using mean value of the resonant and followed antiresonant parameters as the abscissa's value, are almost the same magnitudes as the energy EMCCs k_e. The local maximum energy EMCC k_e for each peak decreases as the exciting frequency increases, in addition, the dynamic EMCC k_d near the resonant and antiresonant frequencies monotonically decreases as the same way. The monotonic increment of dynamic EMCCs is different from that for both free inner and outer surfaces boundary condition [22]. It should be proclaimed that the radial coupling factor k_p for single piezoelectric ring is proper only for static (DC) excitation. In fact, the dynamic EMCC for single piezoelectric ring is quite smaller than the maximum dynamic EMCC for trimorph ring transducer, which composed of two piezoelectric and one elastic rings of the same diameters r_i, r_o, total thickness h, but variable thickness ratio r_i/r_o. The above conclusion can be drawn from experimental impedance

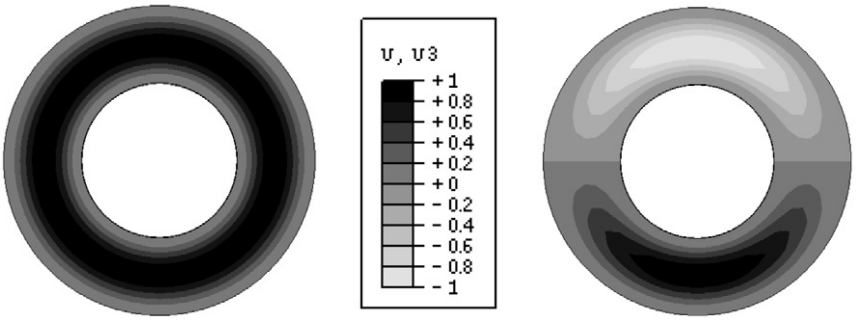

(a) the first resonant frequency: $f_r = 8856.0$ Hz

(b) the second resonant frequency: $f_r = 8964.3$ Hz

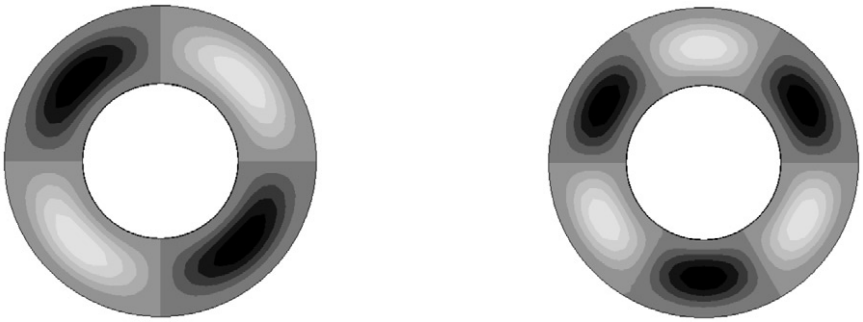

(c) the third resonant frequency: $f_r = 9255.5$ Hz

(d) the fourth resonant frequency: $f_r = 9790.7$ Hz

Fig. 8. The mode shapes with their corresponding resonant frequencies for the fixed inner and fixed outer surfaces boundary condition.

measurements and numerical simulations based on our theories. Since the maximum dynamic EMCC occurs at the vicinity of the first resonant and antiresonant frequencies, we will optimize the trimorph ring transducer for the first dynamic EMCC next. The objective function is to maximize

$$k_d = k_d(r_i/r_o, h_m/h_o, B, D_{ij}, R_0) \tag{43}$$

subjected to the particular material combination of piezoceramics Fuji C-82 and metal Al, that is, B, D_{ij}, R_0 are kept constants. The calculated first dynamic EMCC for the fixed inner and free outer surfaces boundary condition is shown in Fig. 11. Fig. 12 shows results for the free inner and fixed outer surfaces boundary condition. The figures show that the first dynamic EMCC has totally different tendency for different boundary conditions. For carefully examining the data in Fig. 11, the maximum first dynamic EMCC of 0.444 exists when the thickness ratio is 0.38 and the radius ratio is 0.46 for the fixed inner and free outer surfaces boundary condition. Similarly examining the data in Fig. 12, the maximum first dynamic EMCC of 0.406 exists when the thickness ratio is 0.34 and the radius ratio approaches one for the free inner and fixed outer

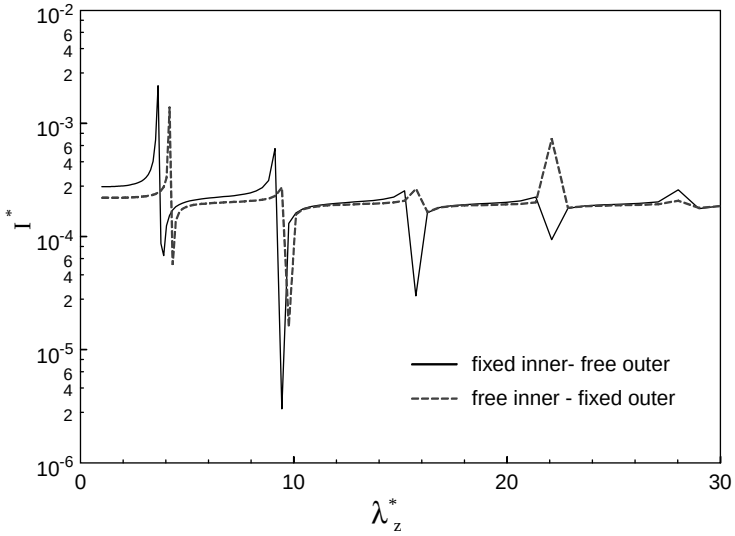

Fig. 9. The non-dimensional electric current responses $I^*\left(I^* = \left[S_{11}^E(1-\nu_p)/\mathrm{j}\pi\omega r_o^2 d_{31}\right]I\right)$ under different exciting frequency parameters λ_z^* for different boundary conditions.

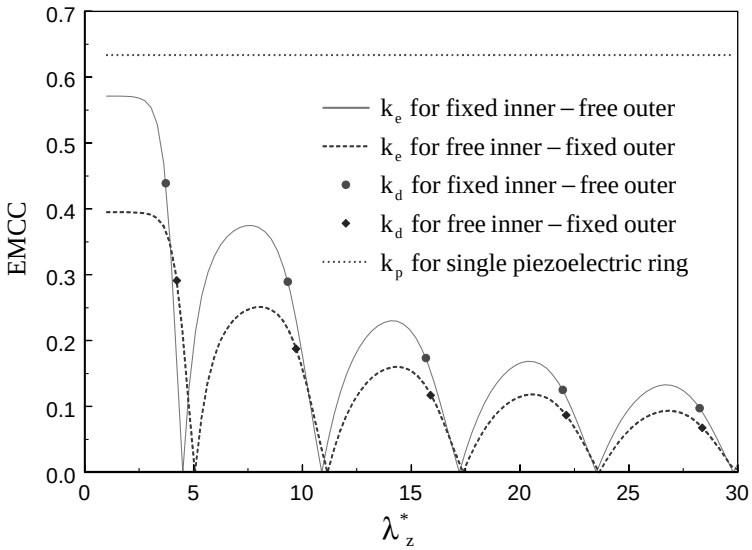

Fig. 10. The dynamic and energy EMCCs under different exciting frequency parameters λ_z^* for different boundary conditions.

surfaces boundary condition. Overall, the trimorph ring transducer for the fixed inner and free outer surfaces boundary condition have slightly lower resonant and antiresonant frequencies and larger EMCCs than those for the free inner and fixed outer surfaces boundary condition. This phenomenon may be due to the bending feasibility in the thickness direction.

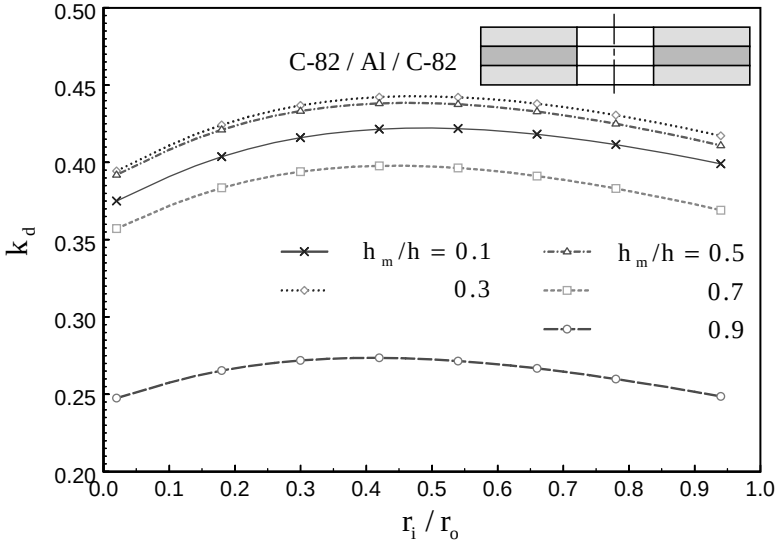

Fig. 11. The first dynamic EMCC k_d versus thickness ratio h_m/h and radius ratio r_i/r_o for the fixed inner and free outer surfaces boundary condition.

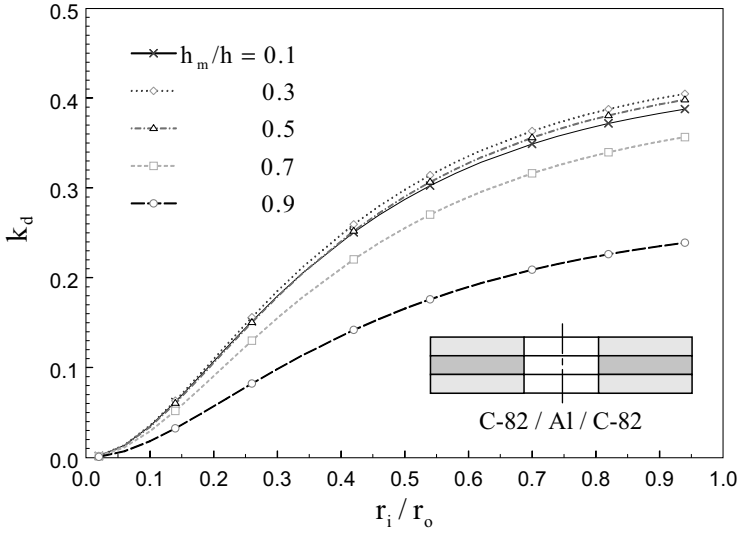

Fig. 12. The first dynamic EMCC k_d versus thickness ratio h_m/h and radius ratio r_i/r_o for the free inner and fixed outer surfaces boundary condition.

5. Conclusions

An electroelastic laminated plate theory is proposed to analyze the dynamic behaviors of the composite piezoelectric/elastic trimorph rings under constant applied voltage and different mechanical boundary conditions, including resonant frequencies, antiresonant frequencies, electric current responses, and dynamic and energy EMCCs. These dynamic characteristics are

then numerically simulated for varying thickness and radius ratios of the piezoelectric and elastic materials by MATLAB. The curves of dimensionless resonant and antiresonant parameters versus radius ratios are figured. With the developed easy-to-use figures, the resonant and antiresonant frequencies of the laminated trimorph ring transducer can be evaluated which would be convenient and useful for transducer design.

The finite element method is also utilized to simulate the resonant, antiresonant frequencies and their corresponding mode shapes. The FEM simulation gathers much more resonant and antiresonant frequencies, which comprise the ones that cannot be excited by electric potential. Only resonant and antiresonant frequencies with their corresponding mode shapes, of which nodal lines are circulars, can be excited by electric potential. Besides, Only above resonant and antiresonant frequencies can be found and form valleys and peaks in the impedance–frequency response diagram. This justifies the electroelastic laminated plate theory, which is formulated based on the concept that the bending motion owing to unequal extensions piezoelectric and elastic rings dominates.

We optimize the trimorph ring transducer using piezoceramics Fuji C-82 and metal Al by maximizing its first dynamic EMCC. Under the optimized configuration, the trimorph ring transducer will reach the maximum dynamic EMCC value 0.444 as the thickness ratio is 0.38 and the radius ratio is 0.46 for the fixed inner and free outer surfaces. And, it will attain the maximum dynamic EMCC value 0.406 as the thickness ratio is 0.34 and the radius ratio approaches one for the free inner and fixed outer surfaces boundary condition. By selecting the appropriate thickness ratio and radius ratio, optimal design of the laminated trimorph ring transducer can be achieved.

Acknowledgements

This work was supported by the National Science Council, Taiwan, Republic of China, under grant number NSC-87-2215-E002-016.

Appendix

Elements of matrix $[A]$ and vector $\{F\}$ in Eq. (32):

For the fixed inner and free outer surfaces boundary condition, elements are zero except:

$$A_{1,1} = \mathrm{J}_0(\lambda_z r_i),\ A_{1,2} = \mathrm{I}_0(\lambda_z r_i),\ A_{1,3} = \mathrm{Y}_0(\lambda_z r_i),\ A_{1,4} = \mathrm{K}_0(\lambda_z r_i),$$

$$A_{2,1} = \mathrm{J}_1(\lambda_z r_i),\ A_{2,2} = -\mathrm{I}_1(\lambda_z r_i),\ A_{2,3} = \mathrm{Y}_1(\lambda_z r_i),\ A_{2,4} = \mathrm{K}_1(\lambda_z r_i),$$

$$A_{3,1} = -\mathrm{J}_1(\lambda_z r_o),\ A_{3,2} = -\mathrm{I}_1(\lambda_z r_o),\ A_{3,3} = -\mathrm{Y}_1(\lambda_z r_o),\ A_{3,4} = \mathrm{K}_1(\lambda_z r_o),$$

$$A_{4,1} = \lambda_z \left[\frac{1}{r_o}(D_{12} - D_{11})\mathrm{J}_1(\lambda_z r_o) + D_{11}\lambda_z \mathrm{J}_0(\lambda_z r_o) \right],$$

$$A_{4,2} = -\lambda_z \left[\frac{1}{r_o}(D_{12} - D_{11})\mathrm{I}_1(\lambda_z r_o) + D_{11}\lambda_z \mathrm{I}_0(\lambda_z r_o) \right],$$

$$A_{4,3} = \lambda_z \left[\frac{1}{r_o} (D_{12} - D_{11}) \mathrm{Y}_1(\lambda_z r_o) + D_{11} \lambda_z \mathrm{Y}_0(\lambda_z r_o) \right],$$

$$A_{4,4} = \lambda_z \left[\frac{1}{r_o} (D_{12} - D_{11}) \mathrm{K}_1(\lambda_z r_o) - D_{11} \lambda_z \mathrm{K}_0(\lambda_z r_o) \right],$$

$$F_{4,1} = -F_{11} V.$$

For the free inner and fixed outer surfaces boundary condition, elements are zero except:

$$A_{1,1} = -\mathrm{J}_1(\lambda_z r_i),\ A_{1,2} = -\mathrm{I}_1(\lambda_z r_i),\ A_{1,3} = -\mathrm{Y}_1(\lambda_z r_i),\ A_{1,4} = \mathrm{K}_1(\lambda_z r_i),$$

$$A_{2,1} = \lambda_z \left[\frac{1}{r_i} (D_{12} - D_{11}) \mathrm{J}_1(\lambda_z r_i) + D_{11} \lambda_z \mathrm{J}_0(\lambda_z r_i) \right],$$

$$A_{2,2} = -\lambda_z \left[\frac{1}{r_i} (D_{12} - D_{11}) \mathrm{I}_1(\lambda_z r_i) + D_{11} \lambda_z \mathrm{I}_0(\lambda_z r_i) \right],$$

$$A_{2,3} = \lambda_z \left[\frac{1}{r_i} (D_{12} - D_{11}) \mathrm{Y}_1(\lambda_z r_i) + D_{11} \lambda_z \mathrm{Y}_0(\lambda_z r_i) \right],$$

$$A_{2,4} = \lambda_z \left[\frac{1}{r_i} (D_{12} - D_{11}) \mathrm{K}_1(\lambda_z r_i) - D_{11} \lambda_z \mathrm{K}_0(\lambda_z r_i) \right],$$

$$A_{3,1} = \mathrm{J}_0(\lambda_z r_o),\ A_{3,2} = \mathrm{I}_0(\lambda_z r_o),\ A_{3,3} = \mathrm{Y}_0(\lambda_z r_o),\ A_{3,4} = \mathrm{K}_0(\lambda_z r_o),$$

$$A_{4,1} = \mathrm{J}_1(\lambda_z r_o),\ A_{4,2} = -\mathrm{I}_1(\lambda_z r_o),\ A_{4,3} = \mathrm{Y}_1(\lambda_z r_o),\ A_{4,4} = \mathrm{K}_1(\lambda_z r_o),$$

$$F_{2,1} = -F_{11} V.$$

For the fixed inner and fixed outer surfaces boundary condition, elements are zero except:

$$A_{1,1} = \mathrm{J}_0(\lambda_z r_i),\ A_{1,2} = \mathrm{I}_0(\lambda_z r_i),\ A_{1,3} = \mathrm{Y}_0(\lambda_z r_i),\ A_{1,4} = \mathrm{K}_0(\lambda_z r_i),$$

$$A_{2,1} = \mathrm{J}_1(\lambda_z r_i),\ A_{2,2} = -\mathrm{I}_1(\lambda_z r_i),\ A_{2,3} = \mathrm{Y}_1(\lambda_z r_i),\ A_{2,4} = \mathrm{K}_1(\lambda_z r_i),$$

$$A_{3,1} = \mathrm{J}_0(\lambda_z r_o),\ A_{3,2} = \mathrm{I}_0(\lambda_z r_o),\ A_{3,3} = \mathrm{Y}_0(\lambda_z r_o),\ A_{3,4} = \mathrm{K}_0(\lambda_z r_o),$$

$$A_{4,1} = \mathrm{J}_1(\lambda_z r_o),\ A_{4,2} = -\mathrm{I}_1(\lambda_z r_o),\ A_{4,3} = \mathrm{Y}_1(\lambda_z r_o),\ A_{4,4} = \mathrm{K}_1(\lambda_z r_o).$$

References

[1] R. Mitra, On the performance characterization of ultrasonic air transducers with radiating membranes, IEEE Transactions on Ultrasonics, Ferroelectrics and Frequency Control 43 (5) (1996) 858–863.

[2] K.Y. Sze, L.Q. Yao, Modeling smart structures with segmented piezoelectric sensors and actuators, Journal of Sound and Vibration 235 (2000) 495–520.

[3] A. Satoh, K. Ohnishi, K. Sakurai, Y. Tomikawa, Experimental considerations on the piezoelectric vibratory gyrosensor using a trident tuning-fork resonator, Japanese Journal of Applied Physics 35 (8) (1996) 4417–4420.

[4] S.H. Chang, Y.C. Tung, A novel design of piezo-driven dual-dimension optical scanning mechanism, Review of Scientific Instrument 69 (9) (1998) 3277–3282.
[5] S.H. Chang, B.C. Du, A precision piezo-driven micropositioner mechanism with large travel range, Review of Scientific Instrument 69 (4) (1998) 1785–1791.
[6] P.V. Luk'yanov, Controlling the acoustic characteristics of a piezoelectric ring using a resonator, International Applied Mechanics 32 (11) (1997) 900–903.
[7] P.C. Macey, Finite element/boundary element modeling techniques applied to ring transducers with viscoelastic coating, Ferroelectrics 187 (1996) 1–4.
[8] H. Hata, Y. Tomikawa, S. Hirose, T. Takano, Ring-form two dimensional (X–Y) moving piezoelectric actuator, Japanese Journal of Applied Physics 35 (9B) (1998) 5023–5026.
[9] J.R. Friend, D.S. Stutts, The dynamics of an annular piezoelectric motor stator, Journal of Sound and Vibration 204 (1997) 421–437.
[10] Y. Kagawa, T. Tsuchiya, T. Kataoka, T. Yamabuchi, T. Furukawa, Finite element simulation of dynamic responses of piezoelectric actuators, Journal of Sound and Vibration 191 (1996) 519–538.
[11] A. Iula, N. Lamberti, M. Pappalardo, A model for the theoretical characterization of thin piezoceramic rings, IEEE Transactions on Ultrasonics, Ferroelectrics, and Frequency Control 43 (3) (1996) 370–375.
[12] S.H. Chang, Y.C. Tung, Electro-elastic characteristics of asymmetric rectangular piezoelectric laminae, IEEE Transactions on Ultrasonics, Ferroelectrics, and Frequency Control 46 (4) (1999) 950–960.
[13] S.Y. He, W.S. Chen, Z.L. Chen, A uniformizing method for the free vibration analysis of metal-piezoceramic composite thin plates, Journal of Sound and Vibration 217 (1998) 261–281.
[14] J.H. Kang, A.W. Leissa, Three-dimensional vibrations of thick, linearly tapered, annular plates, Journal of Sound and Vibration 217 (1998) 927–944.
[15] P.R. Heyliger, G. Ramirez, Free vibration of laminated circular piezoelectric plates and discs, Journal of Sound and Vibration 229 (2000) 935–956.
[16] P.C.Y. Lee, R. Huang, X. Li, W.-H. Shih, Vibrations and static response of asymmetric bimorph disks of piezoelectric ceramics, IEEE Transactions on Ultrasonics, Ferroelectrics, and Frequency Control 47(3) (2000) 706–715.
[17] T. Kaneko, T. Ohmi, N. Ohya, N. Kawahara, A compact and quick-response dynamic focusing lens, Sensors and Actuators A 70 (1998) 92–97.
[18] P.K. Mehta, Moment actuator influence function for flat circular deformable mirrors, Optical Engineering 29 (10) (1990) 1213–1222.
[19] N.N. Rogacheva, The Theory of Piezoelectric Shells and Plates, CRC Press, Boca Raton, FL, 1994.
[20] S.H. Chang, B.C. Du, J.F. Lin, Electro-elastic modeling of annular piezoceramic actuating disk transducers, Journal of Intelligent Materials Systems and Structures 10 (5) (1999) 351–429.
[21] W.P. Mason, Physical Acoustics, Principles and Methods, Vol. 1, Part A, Academic Press, New York, 1964, pp. 169–270.
[22] S.H. Chang, J.F. Lin, Dynamic analysis and optimization of piezoelectric/elastic laminated trimorph ring transducer, IEEE Transactions on Ultrasonics, Ferroelectrics, and Frequency Control, submitted.
[23] R.D. Blevins, Formulas for Natural Frequency and Mode Shape, Van Nostrand, New York, 1979.